


RESEARCH ARTICLE

Open Access



Detection, counting and characterization of nanoplastics in marine bioindicators: a proof of principle study

Andrea Valsesia^{1*} , Jeremie Parot^{2,3}, Jessica Ponti¹, Dora Mehn¹, Rita Marino⁴, Daniela Melillo^{4,5}, Shin Muramoto², Mike Verkouteren², Vincent A. Hackley² and Pascal Colpo¹

Abstract

Plastic particulates in the environment pose an increasing concern for regulatory bodies due to their potential risk to higher organisms (including humans) as they enter the food chain. Nanoplastics (defined here as smaller than 1 μm) are particularly challenging to detect and analyze at environmentally relevant concentrations and in biological matrices. The tunicate *Ciona Robusta* is an effective bioindicator for microplastics and nanoplastic contamination in the marine environment, due to its capacity to filter substantial volumes of water and to accumulate particulates. In this proof-of-principle study that demonstrates a complete methodology, following controlled exposure using spiked samples of a model nanoplastic (100 nm diameter polystyrene spheres) the nanoparticles were separated from an enzymatically digested biological matrix, purified and concentrated for analysis. The described method yields an approximate value for nanoplastic concentration in the organism (with a limit of detection of 10^6 particles/organism, corresponding to 1 ng/g) and provides the chemical composition by Raman spectroscopy. Furthermore, this method can be extended to other biological matrices and used to quantitatively monitor the accumulation of nanoplastics in the environment and food chain.

Keywords: Plastic, Nanoparticles, Environment, Characterization, Detection

Introduction

The release of plastic into the environment is universally recognized as a major threat not only for terrestrial and marine ecosystems, but potentially also for human health [1]. This concern is primarily related to the degradation of plastic materials into micro- and nano-size particulates that can more easily bioaccumulate [2]. Their growing presence in the environment is raising concerns at the global level [3, 4] about the potential risks for human health [5, 6] via contamination of food, water, soil and air [7–9]. Typical of emerging research fields, a harmonized classification of environmental nano-, micro- and meso-plastics remains a topic of

debate [10]. In recent years, substantial research has been devoted to the study of microplastics in the environment [11–13]. Well-known sampling protocols and analytical physical-chemical characterization techniques acquired in other application fields [11, 14], can be applied. However, when considering the presumed fragmentation of microplastic objects down to the nano-scale, the full characterization remains a significant analytical challenge [15, 16]. For instance, at the submicrometer scale, matrix effects and surface contamination contribute additional difficulties to the analytical tasks.

For purposes of the present work, polymeric objects of anthropogenic origin, distributed in the size range between 1 nm and 1000 nm, dispersed in an environmental matrix and presenting colloidal behavior are classified as nanoplastics [17]. Analytical investigations on such systems are intrinsically complex due to the lack of reliable

* Correspondence: Andrea.VALSESIA@ec.europa.eu

¹European Commission, Joint Research Centre (JRC), Via E. Fermi 2749, 21027 Ispra, VA, Italy

Full list of author information is available at the end of the article

sampling [18] and direct identification methods [19] that can deliver quantitative information such as nanoplastic number density, size distribution and polymer chemistry.

Moreover, detection of nanoplastics in the environment is extremely difficult due to their low concentration relative to other substances of interest. Only a few papers have been published so far addressing the quantification of nanoplastics in real environmental samples [9, 20, 21]. For example in the paper [20] environmental levels of nanoplastics were shown in the of the order of a few ng/ml. When these levels of contamination are present in complex matrix they become extremely difficult to be detected. A possible solution to increase the concentration of nanoplastics in complex matrices is the use of bioindicators.

In this context, the use of bioindicators is a convenient methodology to monitor the nanoplastic pollution in a marine environment due to their capacity to take up and concentrate nanoscale particles. Ascidians, or sea squirts, the largest and most diverse class of the sub-phylum Tunicata (also known as Urochordata), are particularly interesting for this purpose, being sessile and filter feeders with great particulate retention ability [22, 23]. Even though food concentration is an important parameter affecting the filtration rate, the exposure to high food concentration induces the act of “squirting” that allows the organisms to expel material through the atrial siphon, thus preventing clogging of the branchial sac. While the turbidity (suspended load) is sensed by ascidians, the nature of particles cannot be discriminated, as they are mucus net feeders. In fact, studies on particle retention efficiency showed that smaller particles are retained at a lesser rate, due to the mucus net porosity [24]. However, as the branchial cavity is connected to the visceral cavity by pharyngo-epicardiac openings [25], we have decided to test the ascidian *C. Robusta* also for retention of PS escaped from mucus net. Speaking from an analytical perspective, suitable methods for the separation and purification of nanoparticles from the organisms are works in progress. The use of chemical digestion by oxidizing, acidic or basic media to digest biological matrices has been reported to degrade some, though not all, plastics present in samples [26]. Fortunately, enzymatic digestion provides a reasonable compromise between digestion efficiency and sample integrity [27]. Unfortunately, enzymatic digestion leaves some of the digested matrix in the form of particulates in the nanoscale size range. This residual material can interfere with the purification and analysis of the target nanoplastics. As such, an additional isolation step is necessary to separate the nanoscale plastic components from the biogenic and non-biogenic residue prior to analysis.

In this context, asymmetrical-flow field flow fractionation (AF4) combined with multiple on-line detectors (MD-AF4) is a highly effective approach that overcomes some limitations of more traditional separation and characterization approaches (e.g., size exclusion chromatography), especially for complex samples. Recent papers have demonstrated the potential of AF4 for the separation of nanoplastics (mostly above 200 nm) [18, 28–30]. In MD-AF4, particle separation is based on analyte diffusion counterbalanced by the perpendicular hydrodynamic force provided by cross-flow through the membrane. In this way, discrete particle populations can be separated, detected, characterized, and approximately quantified on a single experimental platform. Compared with other separation-based methods, AF4 is also particularly effective in handling complex matrices, a clear advantage for analysis of samples derived from biogenic sources [31, 32]. Moreover, the collection of fractions enables off-line analysis by microscopic and spectroscopic techniques for a full characterization of the sample, as we will show in this work.

Here we present an original approach to isolate nanoplastics starting from live bioindicators and enabling nanoplastic detection, counting and identification on-a-chip. *C. Robusta* individuals were exposed to different concentrations of nanoplastic (polystyrene, PS spheres), dispersed in seawater, for a time period sufficient to filter the entire sample volume. After harvesting and pre-treating the ascidian individuals, they are enzymatically digested. Then the samples are fractionated and characterized by MD-AF4 which has been used mainly as a preparative technique to remove by filtering through the semi-permeable membrane a maximum of digested organic compounds and finally to retain, fractionate and characterize the nanoplastic particles for the next steps. Each collected fraction is then spotted onto a surface-functionalized chip in order to estimate the number concentration of particles present in the whole individual. Finally, Raman microscopy allows the unequivocal chemical identification of the nanoplastic.

Materials and methods

Ciona Robusta exposure experiments

As preliminary experiments, three different concentrations of 100 nm diameter Fluoresbrite YG microspheres (Polysciences, Warrenton, PA USA)¹, with an initial concentration at 4.55×10^{13} particles per mL, were tested and for each nanoparticle concentration, three individual *C. Robusta*, kept in different beakers, were used and checked under a fluorescence microscope at 4 time

¹The identification of any commercial product or trade name does not imply endorsement or recommendation by the National Institute of Standards and Technology

point intervals (15 min, 30 min, 1 h, 2 h). The experiments with fluorescent particles confirmed that *C. Robusta* can internalize and accumulate the nanoplastics in the gonads.

Next, experiments with non-fluorescent 100 nm diameter PS (Polyscience) were conducted to develop and evaluate the preparation, fractionation and analysis processes. Briefly, an adult specimen, incubated in 300 mL of filtered (0.22 μm) natural seawater (FSW, with the following composition Cl 55.07%, Na 30.60%, Sulfate 7.72%, Mg 3.68%, Ca 1.17%, K 1.1%) was exposed for 2 h to each of the four increasing concentrations of 100 nm PS: A = 4.55×10^8 particles/mL, B = 4.55×10^9 particles/mL, C = 4.55×10^{10} particles/mL and D = 4.55×10^{11} particles/mL, while one specimen was kept under similar conditions without exposing to PS. Then the individuals were rinsed and manually the tunica was separated from the *C. Robusta* in FSW and homogenized in sterile DI water. A mix of antibiotics (Sigma-Aldrich, P0781) was added to the homogenate to prevent bacterial contamination before storage at 4 °C.

Sample enzymatic digestion

Samples containing one organism in 1 mL FSW, for each exposure condition, were thawed, cut, ultra-sonicated and incubated under stirring overnight at 50 °C in presence of papain solution as part of the protocol previously described [33]. After incubation, sodium dodecyl sulphate (SDS, Sigma-Aldrich) was added at a mass fraction of 2%. Each sample was then centrifuged for 15 min at 13600 rpm to form a pellet. The pellet was then washed twice with ultrapure water.

Prior to the AF4 separation/detection, pellets were redispersed in the corresponding supernatant. The final volume of sample per each condition was 1 mL. Before injection in the AF4 system, samples were filtered through 1.2 μm cellulose acetate filters (Amicon® Ultra) to remove any large aggregates of particles and other large residual material.

All laboratory equipment and materials used during the digestion procedure were thoroughly rinsed with pre-filtered DI water and all solutions were passed through a 0.22 μm pore size filter before use to avoid sample contamination.

AF4 separation and fraction concentration, and purification

Calibration of size versus retention time was performed using NIST Traceable™ PS size standards purchased from ThermoFisher (Fremont, CA). A DualTec Eclipse AF4 instrument (Wyatt Technology, Santa Barbara, CA) equipped with degasser (Gastorr TG-14, Flom Co., Ltd., Tokyo, Japan) and a 1100-series isocratic pump (Agilent Technologies, Santa Clara, CA), an autosampler (Agilent

1260 ALS series) and a refrigerated fraction collector (Agilent 1260 Infinity II Analytical). The system is equipped with three principal detectors, an Agilent 1200 series UV-Vis absorbance diode array detector (DAD) and a multi-angle light scattering (MALS) detector (Wyatt DAWN HELEOS II+). Online DLS measurements were performed using a Wyatt QELS (dynamic light scattering) integrated directly with the MALS array at an angle of 99.9°. In this study, UV absorbance was monitored at 254 nm, though it is possible to measure real-time spectra using the DAD. The MALS intensity calibration was performed using a solution of bovine serum albumin.

AF4 measurement conditions were as follows:

- 1 mmol/L NH_4NO_3 mobile phase
- Short AF4 channel, 145 mm
- 350 μm mylar trapezoidal spacer
- 30 kDa regenerated cellulose membrane
- Injection volume 250 μL

The elution program is detailed in Table S1 in the Supplementary Material. Radius of gyration was determined using the MALS data and applying the Berry model of the Debye plot in the Astra software [34]. MD-AF4 data was analyzed using Agilent OpenLab and Wyatt Astra 6.1.4.25 software. Fractions collected following AF4 separation and online analysis were then concentrated first using an Amicon® Ultra-4 centrifugal filter unit (Ultracel-100 regenerated cellulose membrane, 4 mL volume, UFC810024) to (200 to 300) μL , and then finally using an Amicon Ultra-0.5 centrifugal filter unit (Ultracel-10 regenerated cellulose membrane, 0.5 mL volume, UFC501024) to (20 to 30) μL . Corollary experiments with 100 nm PS particles using UV absorbance showed high recovery ($\geq 95\%$) along this concentration step.

Manual spotting

Manual spotting was performed by pipetting 1 μL solution on different surfaces to create droplets. To avoid droplet evaporation and to limit the formation of a “coffee ring”, samples were incubated in a closed box at 4 °C at a relative humidity $> 85\%$, for the duration of the exposure time, and then rinsed with DI water (the chip was immersed in a volume of 10 mL DI water in a beaker and shaken for 2 min) to remove the non-electrostatically bound particles and/or any persistent post-digestion biological matrix products.

Microspotting system for method development

We used a piezoelectrically actuated inkjet dispenser (Microfab Technologies, Plano, TX, USA) with a nozzle orifice diameter of 50 μm to obtain well-characterized

microdroplets of aqueous solutions and suspensions. We followed inkjet printing methods detailed by Verkouteren [35] with some changes— notably a “dip and sip” procedure for filling the dispenser with the limited amount of prepared fluid. An inspection camera with a zoomable magnification lens and oblique lighting allowed the nozzle to be positioned precisely either over a well in a microplate or the target area of a substrate using the joystick function of the motion controller.

First, a 100 μL aliquot of the prepared fluid was pipetted manually into a well and placed into the printing chamber, where the dispenser nozzle was carefully positioned and dipped fully into the fluid. A slightly negative back-pressure was applied to draw the fluid up into the dispenser.

Gravimetric system

We measured the average droplet mass by moving the dispenser to a sub-microgram balance. A weighing vessel partially filled with water was placed on the balance. Repeatedly, five thousand droplets were dispensed into the weighing vessel at 100 Hz while a data collection script recorded the time and mass reading approximately every second. The average droplet mass was calculated after correcting the mass measurements for evaporation. An exhaustive assessment of uncertainty indicates that droplet mass (in the range of 50 ng to 150 ng) determined by this method is known to better than 1% relative expanded ($k = 2$) uncertainty [35].

Microspotting for Raman spectroscopic analysis

Microspotting for Raman spectroscopic analysis was performed by an automated piezoelectric microarrayer (S3 sciFLEXARRAYER, Scienion AG, Germany). The substrate was placed on a hot plate, pre-heated to 80 °C and kept at stable temperature under atmospheric (non-controlled) humidity conditions during the full spotting procedure. Drop frequency was set to 10 Hz, the nozzle was filled with 10 μL sample and 30,000 drops with a nominal volume of about 0.4 nL were deposited to the same location on the superhydrophobic chip. The spotted material was spectroscopically analyzed without any further treatment by Raman microscopy.

Confocal Raman spectroscopic analysis of the spotted sample was performed using a WITec alpha300 confocal Raman microscope (WITec, Germany), equipped with a 533 nm laser. Optical images of the spot were taken using a 10x objective, while chemical mapping of the area of interest was performed with a 100x objective at 500 nm resolution using a piezo stage. An integration time of 10 s was applied for the collection of spectra at each pixel. Spectral images were baseline subtracted and processed with the Basis Analysis function of the WITec

Project software. A sample consisting of N different materials shows a linear superposition \vec{S} of all its basis spectra.

$$\vec{S} = \sum_{k=1}^N a_k \vec{B}_k \quad (1)$$

If the basis spectra \vec{B}_k of the pure materials are known, the weighting factors a_k are estimated by a least square fit.

The reference spectrum \vec{B}_k of polystyrene used in the calculations was collected earlier with the same instrument using a 10x objective and at 10×10 s integration time, using a polystyrene sheet purchased from Goodfellow (Huntingdon, England) Identification of cellulose acetate particles was performed using the UVIR Manager software of ACDLabs (Toronto, Canada) and a lab-constructed polymer database.

Surface modification

10 cm Si (100) wafers were diced into 15 mm \times 15 mm square pieces using a dicing saw equipped with a 15 μm diamond-impregnated metal blade and cleaned sequentially in a sonicated bath for 5 min in methylene chloride, acetone, and methanol to remove organic contaminants. To create a hydrophilic surface, Si pieces were immersed in a 3:1 ($\text{H}_2\text{SO}_4\text{:H}_2\text{O}_2$) Piranha solution for 10 min, rinsed in ultrapure water, and dried under a stream of liquid nitrogen (Safety note: Piranha is highly corrosive and an extremely powerful oxidizer. Use proper safety gear, and always pour H_2O_2 into the acid, never in reverse). The treatment creates a hydrophilic surface with a water contact angle (WCA) of roughly 20°. To create a hydrophobic surface, a thin layer of a low-energy fluorocarbon was self-assembled onto the Si surface by molecular vapor deposition, where the Si pieces were exposed overnight to 5 mg of 1H,1H,2H,2H-perfluorodecyltrichlorosilane (FDTS) (Alfa Aesar, Ward Hill, MA) inside a small plastic container. This creates a hydrophobic surface with a WCA of roughly 110°. To create a superhydrophobic surface (WCA > 130°), the cleaned Si pieces were etched in a 80 °C bath of 3% mass fraction KOH and 5% volume fraction isopropyl alcohol in water for 30 min to introduce micro- and nanostructures on the surface. A low-energy chemistry was then added to the surface using the same FDTS chemistry and self-assembly mentioned above. The modification of the surfaces to generate a positive charge was made by dip coating of poly (diallyldimethylammonium chloride), PDDA (Sigma Aldrich, CAS Number 26062–79–3), at a concentration of 4% volume fraction in filtered high purity DI water.

SEM/EDX and image analysis

Scanning electron microscopy was performed using an environmental SEM (ESEM) (ThermoFisher- The Netherlands) working at low pressure, equipped with a Bruker (Germany) Energy Dispersive X-Ray (EDX) analyzer. The measurement for the surface density was obtained by SEM imaging of the droplet footprint in combination with ImageJ software analysis (<https://imagej.nih.gov>). The analysis was performed using the Analyze Particles Function of ImageJ, nanoparticle boundaries were identified as red stains on a black background and only those with a size between 100 and 200 pixel units and circularity value between 0.80 and 1.00 were taken into account for the coverage degree calculation. The number of particles measured per each exposure condition was calculated as the average of three images collected at different locations inside the droplet footprint. The uncertainty for the measurement of the number of particles was calculated as the standard deviation obtained from the calculation of number of particles on the three images.

Some images have been acquired using a field emission SEM (FESEM), Nova600i Nanolab (Thermofisher-The Netherlands).

Results and discussion

C. *Robusta* exposure to PS and enzymatic digestion

The preliminary experiments using fluorescent labelled PS spheres were aimed at selecting a range of doses and exposure times to ensure detectable PS particles in the *C. Robusta*. The experiments with fluorescent particles confirmed that *C. Robusta* internalizes and accumulates the PS nanoparticles in the gonads (Fig. 1b and c). Figure 1a shows the corresponding bright field image.

Accumulation of PS in the organism increased with both exposure time and concentration as expected (data not shown). Similarly, *C. Robusta* was exposed for 2 h to each of four increasing concentrations of the non-fluorescent 100 nm PS spheres (from 4.55×10^8 /mL to

4.55×10^{11} /mL), and one organism was kept under similar conditions, but without PS, as a control. Following homogenization, digestion and pre-filtering, the resulting samples were ready for fractionation and analysis.

AF4 fractionation and pellet purification/concentration

The primary objective here was to use AF4 as a preparative technique to isolate and concentrate nanoplastics in a specific size band from a complex medium for offline analysis, not as a stand-alone analytical method. Initially, a MD-AF4 method was applied based on previous experience and following standard practice [36]. This method was then tested and optimized further using four monodisperse PS sphere populations that encompass the size of the exposure material and with nominal diameters of 30 ± 1 nm, 60 ± 4 nm, 100 ± 3 nm and 203 ± 5 nm. The detailed parameters of the final optimized method are reported in supplemental Table S1. Applying this AF4 method, PS particles were fractionated with narrow single elution peaks at distinguishable retention times (Figure S1), t_R , with $t_R = (6.7, 10.5, 15.6$ and $30.2)$ min for (30, 60, 100 and 203) nm particles, respectively. Moreover, the analysis of these four PS samples using the optimized method yielded very high PS recovery ($\geq 95\%$), based on integrating the UV absorbance at 254 nm (with and without focus+cross-flow). As expected, retention time increases with increasing nominal particle size according to diffusion-dominated “normal mode” fractionation operable for particles smaller than about $0.5 \mu\text{m}$. But as particle size approaches the micrometer range, a transition from normal to steric mode will occur, resulting in a reversal of the correlation between size and retention time [37]. Although this transition poses a potential complexity in the AF4 analysis, the optimized method used here generally excludes micrometer size particles, if present, from interfering with the fractionation and isolation of nanoplastics, as the larger particles will be retained under the conditions of this study and only elute after removal of cross-flow.

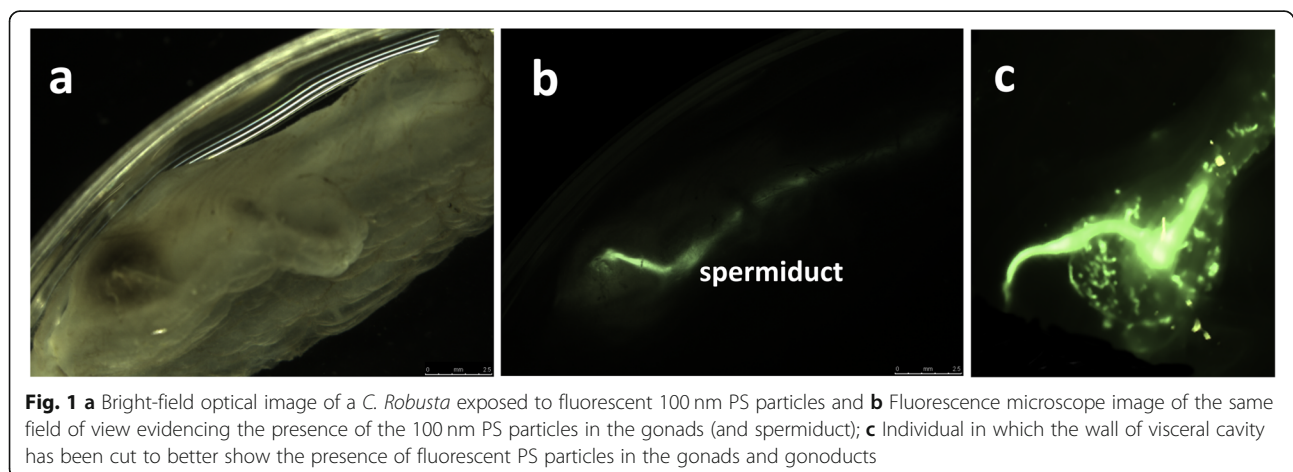


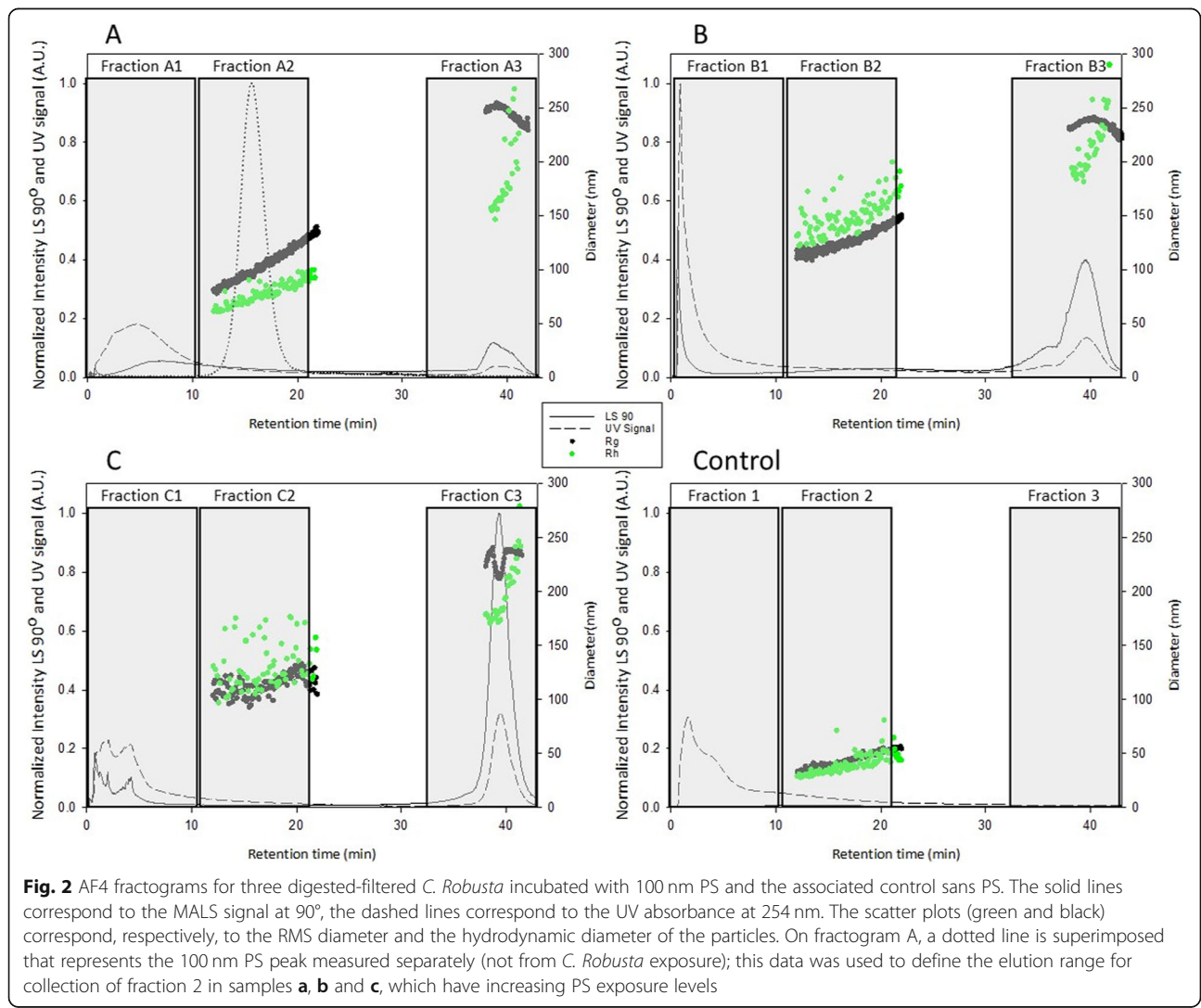
Fig. 1 **a** Bright-field optical image of a *C. Robusta* exposed to fluorescent 100 nm PS particles and **b** Fluorescence microscope image of the same field of view evidencing the presence of the 100 nm PS particles in the gonads (and spermiduct); **c** Individual in which the wall of visceral cavity has been cut to better show the presence of fluorescent PS particles in the gonads and gonoducts

The three online detectors (UV-Vis DAD, MALS, and DLS) together provide a high-resolution characterization of the fractionated “slices” (e.g., UV-Vis absorbance spectra, root mean square (RMS) diameter and hydrodynamic (DLS-based) diameter). Specific fractions are collected for offline analysis over retention times as defined in Fig. 2. The presence of an ultrafiltration membrane in the AF4 channel offers an additional benefit, in that compounds with a molar mass smaller than about 30 kDa (membrane cut-off) are mostly removed through the membrane providing an additional “cleaning” step for complex media that allows for improved analysis downstream. This molar mass cutoff corresponds to proteins smaller than about 5 nm. In the present case, this enables removal of much of the residual organic matter after digestion without loss of the nanoparticles. It should be noted that analyte interactions with the membrane can impact the fractionation process, altering the retention time and decreasing recovery. These

interactions should be assessed and mitigated, if necessary, during method development. In this study, PS spheres did not substantially interact with the membrane, as shown by the high recoveries already reported.

This MD-AF4 optimized method was then applied to digested *C. Robusta* individuals incubated with a known number of 100 nm PS particles (samples A, B and C; sample D is not shown), and one control incubated without PS particles (see Fig. 2). For each sample, a volume of 250 μL was injected into the mobile phase.

For the three exposed samples, two peaks can be distinguished (UV + LS), one immediately after the void peak ($t_R = 0$ min) and another centered at $t_R = 40$ min (i.e., just after cross-flow decays to 0). Between these peaks is a long featureless elution period containing a very low but detectable particle presence that overlaps with the expected retention time range for 100 nm PS (see overlaid, dotted peak in Fig. 2a). On the other hand, there is no detectable LS signal in the control sample,



only UV absorbance due most likely to residual organic species not removed through the membrane, thus confirming the absence of PS. In samples A-C, the LS peak at 40 min shows a sharp increase in intensity that correlates with the increase in PS exposure, suggesting this peak contains agglomerated PS. This is confirmed by the online analysis that yields sizes in excess of 200 nm. By comparison, the fast-eluting smaller peak has a relatively high UV absorbance (compared to LS signal) and is not very consistent or well defined. Given the smaller LS signal present, this peak contains some PS, possibly entrained with the same residual organic matter indicated in the control sample. Our target for this study was the unagglomerated, 100 nm PS particles that we expect to elute between retention times of roughly (12 to 20) min – assigned based on the aforementioned experiments summarized in Figure S1. The online RMS and DLS diameters measured across fraction 2 confirm our expectation; the measured size is not entirely consistent here, though it suggests a diameter close to 100 nm. The lack of consistency is due to the low scattering intensity in this range.

Recovery in AF4 is determined using a mass sensitive online detector with and without focus+cross-flow, in this case by integration of UV absorbance at 254 nm. For samples A, B and C, recovery was quantified in this manner, but a substantial portion of the UV absorbance is due to residual organic matter resulting from sample digestion (i.e., not PS analyte alone). Hence, for A, B and C the recoveries were 13%, 12% and 20%, respectively. While these numbers are well below generally acceptable recovery for AF4 (70%) [38], in this case it actually reflects the efficiency with which low molecular mass residues from digestion are removed during analysis; the UV absorbance without focus+cross-flow is very high relative to absorbance during fractionation due to the residual material in the complex media (thus the low calculated recoveries).

Following AF4 separation and as highlighted in Fig. 1, fractions were automatically collected at retention times associated with the initial peak (fraction 1), the 100 nm PS (fraction 2) and the final peak (fraction 3). Each AF4 fraction, consisting of a volume of 5 mL, was purified and concentrated using 0.5 mL regenerated cellulose centrifugal filters with a cutoff at 10 kDa; this step provided a 200x concentration of the samples to bring the final volume to 25 μ L. Considering an AF4 injected sample volume of 250 μ L at the beginning of the process, we obtain a concentration factor of 10x at the end of this process. This concentration factor has been considered for the estimation of the concentration of PS particles in the next steps of the analysis. A quantitative assessment of all potential losses and evaluation of the concentration efficiency will be performed in future work that

focuses on validation of the methodology and application to other nanoplastics including materials derived from marine environments; this is beyond the scope of this proof of principle study.

Particle ordering on the surfaces by manual and microspotting

The controlled deposition of the concentrated AF4 fractions onto the functionalized chip was performed by manual spotting and by microspotting. While the former involves manually pipetting a small volume of the sample (< 1 μ L) directly onto a chip, the latter uses a piezoelectric micro-nozzle driven by a waveform generator that produces very small droplets of around 80 pL.

Water contact angle (WCA) of the chip surface plays an important role in the process. Surfaces characterized by low values will induce the spreading of the droplet, with a consequent increase of the droplet footprint diameter (α). In this work, we compared α from three functionalized chips: 1) An oxidized Si wafer dip coated with positively charged poly (diallyldimethylammonium) chloride (PDDA) (SiO₂-PDDA, CA < 20°), 2) an as-received silicon dip coated with PDDA (Si-PDDA, CA = 50°), 3) A perfluorodecyltrichlorosilane (FDTS)-coated Si wafer that was subsequently dip coated with positively charged PDDA (Si-FDTS-PDDA, CA = 85°. The surface polarity (defined here as the sign of the streaming potential at pH = 7) is important for inducing a controlled adsorption (immobilization) of the nanoparticles to the collector surface by electrostatic forces. The water angle parameters of the different surfaces are summarized in Table S2.

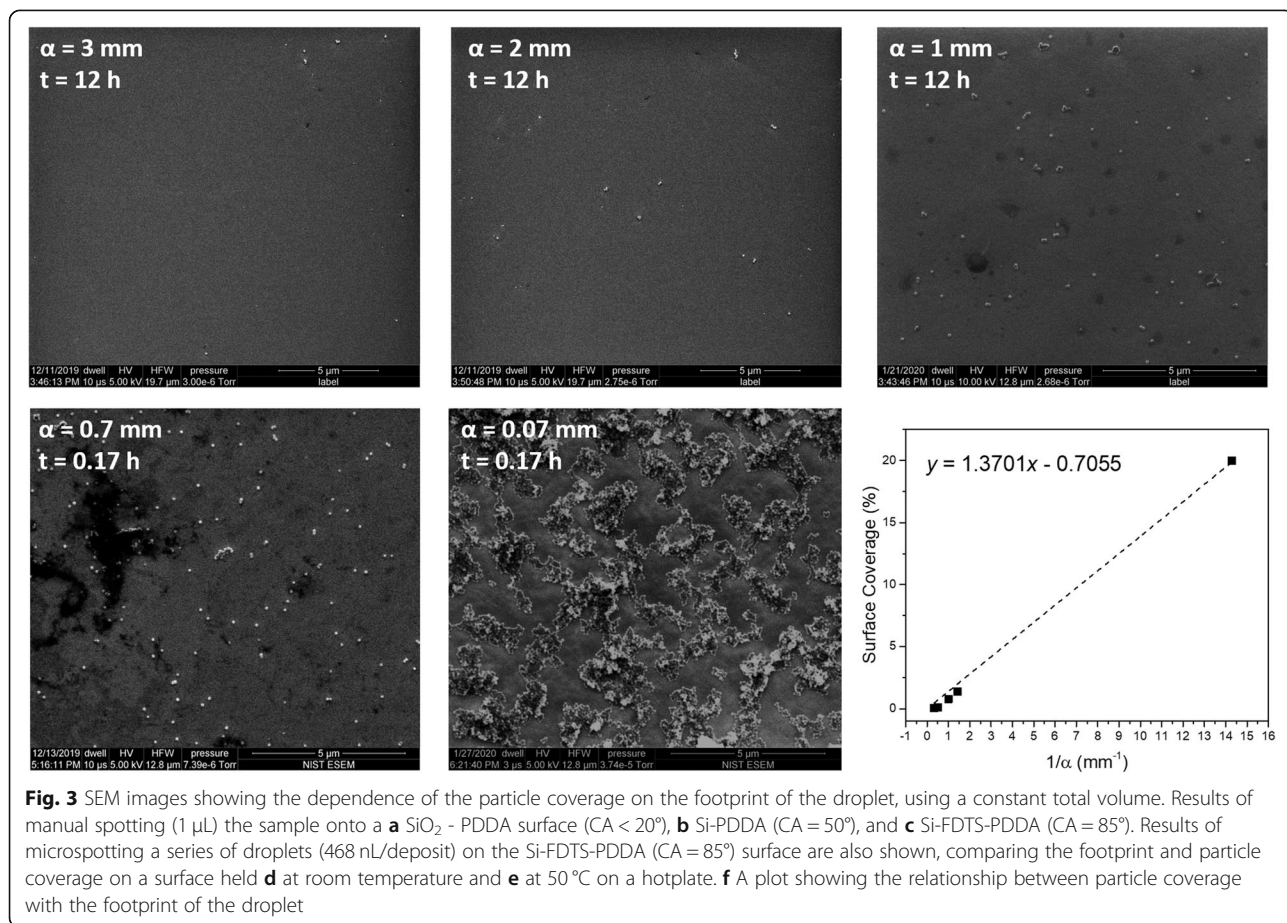
When a liquid containing nanoparticles is in contact with a chip surface their adsorption depends on two physical limitations: energetics favorability and transport kinetics. The first effect is regulated by the extended Derjaguin-Landau-Verwey-Overbeek (XDLVO) theory [39], governing the energetics of adsorption between particles and a surface. Under the previously described conditions, the surface density of particles immobilized on the surface is N_s/S , where

$$N_s = C_0 \sqrt{tK_B T / 12\pi\eta r} \quad (2)$$

and S is the observed area. In Eq. 2, C_0 is the particle concentration in the bulk medium, t is time, $K_B T$ is thermal energy, η is the viscosity of the medium and r is particle hydrodynamic radius. From this equation, the number of particles deposited at a constant temperature for a given medium (typically water) over a fixed time period is proportional to the bulk concentration. Due to the separation process in AF4, individual fractions generally contain nearly monodisperse particle populations with respect to hydrodynamic size [40]. The model is

valid for an ideally monodispersed suspension of particles in a medium characterized by a certain viscosity. Higher particle density is obtained primarily by controlling the particle-surface interaction and limiting the size of the droplet footprint. The particle surface density is relatively homogenous inside the footprint of the droplet, since the formation of a “coffee ring” is limited by avoiding the evaporation of the droplet during the incubation time (see [Materials and methods](#) section). A representative SEM image of particles distributed over the surface near the boundary of a droplet is shown in Figure S4. Particle surface density as a function of droplet footprint is shown in Fig. 3. The droplet footprint is controlled by the wettability of the chip. The footprint diameter (α) equal to (3, 2 and 1 mm (Fig. 2a, b, c respectively) is obtained by manual spotting 1 μ L of suspension on SiO₂-PDDA (CA < 20°), as received silicon-PDDA (CA = 50°) and silicon-FDTS-PDDA (CA = 85°). Within uncertainty, the observed differences in surface density (Fig. 3a, b and c) are only due to the footprint of the droplet, given that surface charge and contact time are the same for the three surfaces.

To further reduce the footprint and to increase the areal density, a microspotter was evaluated to produce much smaller droplets. For example, by dispensing a series of small droplets over a 10 min period, using a frequency adjusted to the evaporation rate of the droplets, the particle coverage was successfully increased by a factor of 2 through a 50% reduction in α (Fig. 3d). Further reduction in α was observed by increasing the surface temperature, in this case to 50 °C, by using a hotplate during deposition (Fig. 3e). By instantly evaporating the droplet upon deposition, an area of about 4000 μ m² was achieved. An optical image of the droplet and the evolution of the droplet with time is shown in Figures S5a and b, respectively. This is the smallest footprint obtained on the Si-FDTS-PDDA surface. The droplets are ejected at a frequency of 10 Hz and instantaneously evaporate when they impinge on the hot surface. In this way, the droplet footprint area is kept relatively constant through the duration of the dispensing process. As can be seen in Figure S5a and b, the evolution of the footprint is very small, around 3×10^{-5} mm²/min, making the technique useful for dramatically increasing the areal density of the particles.



At a particle concentration between 10^6 and 10^{10} per mL (corresponding to an equivalent mass of PS of 0.5 ng and 5000 ng per mL), the surface coverage obtained by microspotting can be detected by SEM (data not shown).

Measurement of PS concentration in the exposed *C. Robusta* samples

The calibration solutions consist of 100 ± 3 nm PS spheres dispersed, at different concentrations, in a digested sample of *C. Robusta* not previously exposed to PS in the laboratory. The measurement of PS particle concentration in the exposed *C. Robusta* samples was determined by manually spotting the concentrated fractions on the silicon-FDTS-PDDA functionalized chip. The 1 μ L droplets were incubated for 12 h on the chip surface, together with the calibration solutions. The results for the different fractions are shown in Fig. 4. For each fraction, the number of particles bound to the surface is proportional to the particle concentration in the bulk. Fraction 2 (C_2 , B_2 , A_2) contains particles having a diameter of about 100 nm, as demonstrated by the preliminary AF4 experiments. This procedure enables the maximization of the number of particles reaching and binding to the surface, as shown in the previous section.

The set of calibration concentrations is shown in Figure S2.

The concentration of particles in the fractions is calculated by the following equation:

$$[C]_{fraction} = \frac{1}{10} k N_{fraction} \quad (3)$$

where $N_{fraction}$ is the number of particles counted by SEM on the surface of the collector (counting made by image analysis software, details in the [Materials and methods](#) section), k is the calibration constant measured for the concentration series of PS beads. The value is divided by 10, which is the concentration factor obtained after the AF4 analysis.

In the present study, $k = 1.6 \times 10^6$ /mL. The factor k was calculated by the linear fit of the calibration curve (Figure S3). Using these values, the concentration of PS particles in the exposed *C. Robusta* samples at the different doses are calculated and shown in Table 1, which shows the original concentration of PS to which the organism was exposed in the experiment, the total number of particles passing by the organism filters (calculated as the particles contained in the volume of water where the organism has been incubated – since during the incubation time the organism is able to filter the entire water volume), the number of particles counted by SEM on the chip, and the concentration in the solution calculated using Eq. 3. Particles are counted on three different equivalent SEM areas and averaged. SEM analysis is shown in Fig. 4. The uncertainty intervals are \pm one

standard deviation for the three SEM image analyses. EDX analysis confirmed that the large majority of detected objects in the fractions (A2, B2, C2 and D2) were PS particles. They contain only carbon as an element, compared to other particles that contain oxygen or other inorganic elements. Examples of detected particles and their assignment are shown in Table S3.

Interestingly, an expected monotonic correlation between the dose of PS and the concentration of PS retained by the *C. Robusta* is not observed. The highest retention of particles corresponds to the *C. Robusta* exposed to a concentration of 4.55×10^9 PS/mL (sample B). We attribute this unexpected result to a different agglomeration state of the particles in the seawater (versus laboratory water), also the behavior of the *C. Robusta* in the presence of high concentrations of particles, leading to turbid conditions, plays an important role. Briefly, a current of water entering from the inhalant syphon passes through the pharynx or branchial sac coated with a mucus net, a mesh-like structure produced continuously by the endostyle [23]. The mucus-gathered particles are continuously transported to the digestive tube, while cleared water passes through numerous stigmata ciliated openings of the pharynx wall into the atrial cavity and eventually is ejected through the exhalant syphon. A visual scheme of the described mechanisms is shown in Fig. 5. Applying this model for the case of PS, for the two highest concentrations of PS, the particle agglomeration and the turbidity likely induces rapid expulsion of the particles by *C. Robusta* (so called squirting), leading to a reduced internalization of particles. The consequent retention is very low (as low as one in every 10^8 particles is retained by the organism). For the two lowest concentrations, the retention of particles is much higher – at least one particle for every 1000 particles is retained by the organism at a concentration of 4.55×10^9 PS/mL. The retention efficiency (number of particles available for the organism/measured particles in the organism) is reported in Table 1. Although further testing and validation is necessary for a complete mass balance, these results suggest that *C. Robusta* is a very good candidate to serve as a bioindicator for PS, since it shows much better retention efficiency at low particle concentration. Low concentrations are more relevant for expected environmental exposure levels. Further studies are needed to confirm this hypothesis. We believe this data represents the first demonstration of Millar's hypothesis that there is an exchange of water between branchial and visceral cavities [41].

Identification of PS by Raman

By using the microspotting technique, we exploited the tendency for nanoparticles to cluster as the droplet dries [42], with their size varying from a few hundred

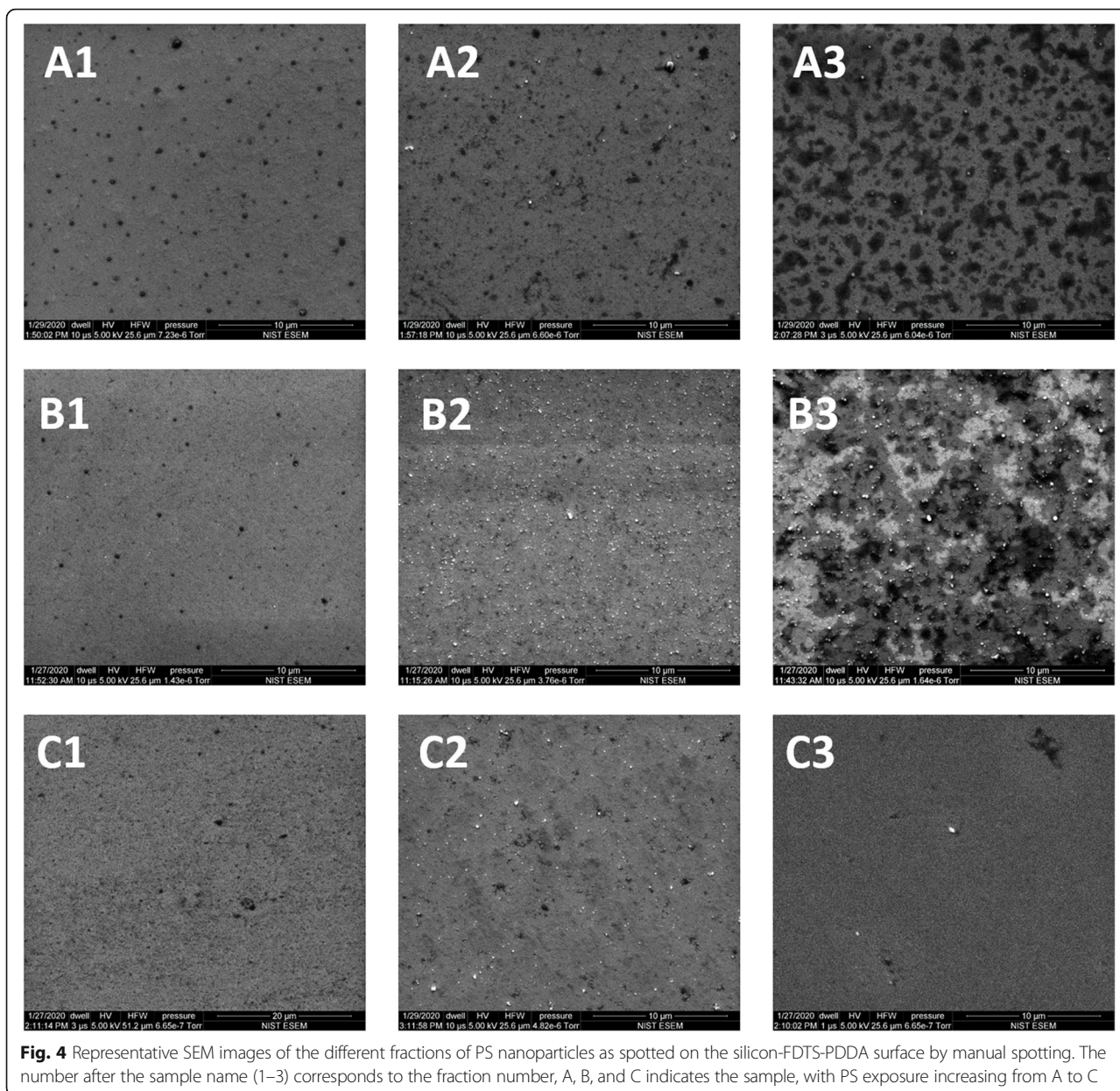


Fig. 4 Representative SEM images of the different fractions of PS nanoparticles as spotted on the silicon-FDTS-PDDA surface by manual spotting. The number after the sample name (1–3) corresponds to the fraction number, A, B, and C indicates the sample, with PS exposure increasing from A to C

Table 1 Summary of the exposure experiments and the calculated concentration of particles retained in the different *C. Robusta* samples exposed to different doses of particles

Sample _{Fraction}	Dose concentration (PS part/mL) ^a	Number of particles available for organism (PS particles)	Counted on chip (n) ^b	Measured concentration (PS part/mL)	Retention efficiency ^c
A ₂	4.55×10^8	1.37×10^{10}	677 ± 17	$(8.1 \pm 0.1) \times 10^7$	5.93×10^{-03}
B ₂	4.55×10^9	1.37×10^{11}	1763 ± 21	$(2.1 \pm 0.1) \times 10^8$	1.55×10^{-03}
C ₂	4.55×10^{10}	1.37×10^{12}	32 ± 5	$(3.8 \pm 0.8) \times 10^6$	2.80×10^{-06}
D ₂	4.55×10^{11}	1.37×10^{13}	4 ± 2	$(4.8 \pm 3.2) \times 10^5$	3.50×10^{-08}

^a The dose concentration of particles has an uncertainty of 15% as declared by the vendor

^b It is possible that surfaces are contaminated with other particles. The very low number of particles counted on chip in sample D₂ is probably too close to the detectable limit of particle, so it can be approximated to zero

^c The Retention Efficiency is calculated as the measured concentration of particles in the fraction and the number of particles available for the organism

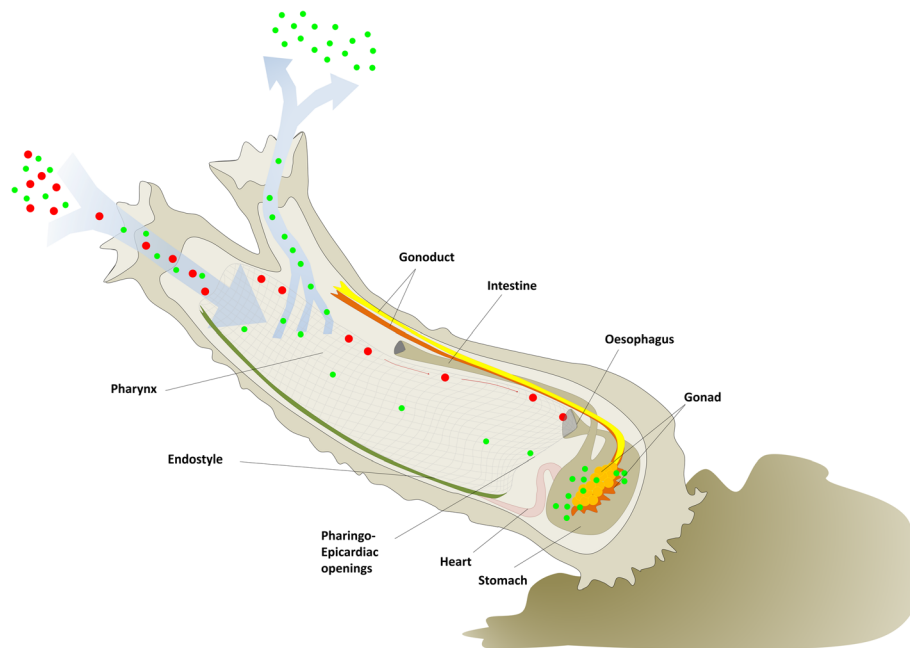


Fig. 5 Schematic representation of an adult individual of *C. Robusta* highlighting water circulation (blue arrows). Incoming particles (red dots), with a size bigger than the mucus net grids, move to the oesophagus. On the other hand, smaller particles (green dots) preferentially pass through the pharynx ostia and they are expelled. Some particles reach the visceral cavity through the pharyngo-epicardiac openings and accumulate in the gonads

nanometers to tens of micrometers, as can be seen in Figures S6a and b. This artefact provided sufficient signal for analysis by conventional Raman confocal microscopy.

The fraction B₂, i.e., the one containing the largest concentration of PS, was microspotted over a superhydrophobic surface to maximize clustering of the particles. A relatively large volume of sample (1.2 μ L) was dispensed onto the same location of a heated surface by a microspotter producing single droplets with a volume of 0.4 nL, at a frequency of 10 Hz.

An area of 625 μ m² (the red area in Fig. 6a) was then scanned by conventional confocal Raman microscopy with steps of 500 nm and an integration time of 10 s per point. Using a known polystyrene spectrum as a reference (Fig. 6b, bottom curve), spectral regions containing characteristic PS peaks were identified using basis analysis in the nanoparticle clusters (Fig. 6b, top curve). Using this information, a 2-channel image was then generated highlighting the pixels containing those characteristic peaks as shown in Fig. 6c.

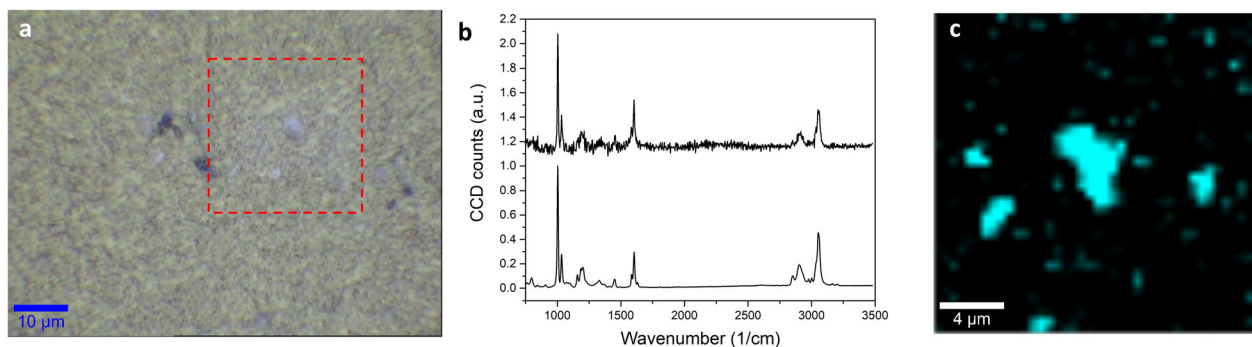


Fig. 6 Confocal Raman microscopy characterization of the microspotted fraction D₂. **a** optical image; **b** typical spectrum of a nanoparticle cluster (top curve) and PS reference (bottom curve), with the light blue spectral zones showing the presence of characteristic PS peaks; **c** color map of the clusters obtained by the base component analysis, identified as PS. In **(a)**, the PS clusters appear light under white light illumination and are present throughout the deposit. The red box in **(a)** represents the scanned area by Raman spectroscopy

Other polymeric objects were also found in the same deposit, and their results are shown in Figure S7. These objects were attributed to cellulose acetate with an 85% match according to an in-house-constructed polymer database. The presence of cellulose acetate nanoparticles could be due to release from the 1.2 μm syringe filters used prior to the AF4 separation.

Conclusions

In summary, there are two main innovative aspects demonstrated in this prototype investigation: the first is the evidence of the behavior of the selected bioindicator, *C. Robusta*, and its ability to internalize and concentrate small polymeric particles ($< 1 \mu\text{m}$) without affecting their size and shape. The second is the multistage method for the extraction and purification of the particles from a complex matrix, enabling their counting and identification. Extraction of the particles is enabled by homogenization followed by enzymatic digestion. Subsequently, isolation/characterization is achieved by MD-AF4. Finally, counting and identification are obtained by an *on-chip* analysis of the isolated and concentrated fractions.

Identification is facilitated by inducing the formation of particle clusters on the chip during the drying of the droplets ejected by a microspotter. The formed clusters are then detectable by conventional confocal Raman spectroscopy. By mapping the footprint of the droplets, it is possible to identify the unique spectrum of the different particles constituting the fraction.

The exposure-preparation-analysis scheme presented here has broad implications for the risk assessment of nanoplastics and microplastics in marine environments. Risk analysis is heavily dependent upon the ability to accurately measure the quantity of species present and to characterize their chemical and physical properties. At the same time, recent articles in the scientific literature and in mass media have consistently emphasized the substantial challenge posed by the need to isolate and measure sub-micrometer plastics at ultra-low concentrations and in complex natural media. In this prototype study we have demonstrated the essential components of a process to address this challenge. Future efforts should focus on further optimizing and validating the methodology. In particular, a more extensive study will allow for precise assessment of LOD, recovery, measurement precision and reproducibility. Extension to other nanoplastic materials is also required for full validation, including environmentally sourced materials.

Abbreviations

AF4: Asymmetric Field Flow Fractionation; *C. Robusta*: *Ciona Robusta*; CRS: Confocal Raman Spectroscopy; DI: Deionized; DLS: Dynamic Light Scattering; EDX: Energy Dispersive X-Rays; ESEM: Environmental Scanning Electron Microscope; FDTs: 1H,1H,2H,2H-

perfluorodecyltrichlorosilane; FESEM: Field Emission Scanning Electron Microscope; FSW: Filtered Seawater; LOD: Limit of detection; MALS: Multi Angle Light Scattering; MD-AF4: Multiple Detector Asymmetric Field Flow Fractionation; PDDA: Poly (diallyldimethylammonium chloride); PS: Polystyrene; RMS: Root Mean Square; SDS: Sodium Dodecyl Sulfate; SEM: Scanning Electron Microscope; WCA: Water Contact Angle; XDLVO: Extended Derjaguin-Landau-Verwey-Overbeek

Supplementary Information

The online version contains supplementary material available at <https://doi.org/10.1186/s43591-021-00005-z>.

Additional file 1.

Acknowledgements

A. Valesia is grateful to A. Hoeweler (JRC – F2) and K. Aschberger (JRC – A5) for their support with the Visiting Research Program to NIST and J. Gorham, D. Holbrook, B. Nelson (NIST) for their welcome in Gaithersburg and their support for this project. Thanks to S. Facchetti for her support in the enzymatic digestion protocol. Thanks to P. Italiani for providing the *C. Robusta* scheme in Fig. 5.

Authors' contributions

A. Valesia designed the experiments, developed the whole protocol, performed SEM, microspotting and Raman analysis, analysed data, wrote the manuscript. J. Parot Designed and performed AF4 experiments and wrote the manuscript. J. Ponti Developed and performed digestion experiments. D. Mehn performed microspotting and Raman analysis. R. Marino designed and performed exposure experiments with *C. Robusta* and wrote the manuscript. D. Melillo performed exposure experiments with *C. Robusta* and sample preparation. S. Muramoto prepared and characterized functionalized surfaces and superhydrophobic surfaces. M. Verkouteren developed the microspotting method for nanoparticles dispensing study. V. Hackley participated to the design of the experiments and wrote the manuscript. P. Colpo participated to the design of the experiments and wrote the manuscript. The author(s) read and approved the final manuscript.

Funding

The project was financed through the JRC proof of concept project "Nanoplastics" and the JRC Visiting Research Program fellowship.

Availability of data and materials

The datasets generated during and/or analysed during the current study are available from the corresponding author on reasonable request.

Declarations

Competing interests

The authors declare no competing interests.

Author details

¹European Commission, Joint Research Centre (JRC), Via E. Fermi 2749, 21027 Ispra, VA, Italy. ²National Institute of Standards and Technology, Materials Measurement Science Division, Gaithersburg, MD 20899, USA. ³Department of Biotechnology and Nanomedicine, SINTEF Industry, Trondheim, Norway. ⁴Biology and Evolution of Marine Organisms (BEOM), Stazione Zoologica "Anton Dohrn", Naples, Italy. ⁵Institute of Biochemistry and Cell Biology, National Research Council, Naples, Italy.

Received: 14 January 2021 Accepted: 26 March 2021

Published online: 15 April 2021

References

1. Vethaak AD, Leslie HA. Plastic debris is a human health issue. *Environ Sci Technol.* 2016;50(13):6825–6. Available from: <https://doi.org/10.1021/acs.est.6b02569>.
2. Wright SL, Kelly FJ. Plastic and human health: a micro issue? *Environ Sci Technol.* 2017;51(12):6634–47. <https://doi.org/10.1021/acs.est.7b00423>.

3. Nyka M. Legal approaches to the problem of pollution of marine environment with plastic. *Sci J Marit Univ Szczecin*. 2019;59(131):162–7.
4. UNEP. Marine litter: a global challenge. United Nations Environmental Programme (UNEP); 2009. p. 234.
5. Lehner R, Weder C, Petri-Fink A, Rothen-Rutishauser B. Emergence of nanoplastic in the environment and possible impact on human health. *Environ Sci Technol*. 2019;53(4):1748–65. <https://doi.org/10.1021/acs.est.8b05512>.
6. Bouwmeester H, Hollman PCH, Peters RJB. Potential health impact of environmentally released micro-and nanoplastics in the human food production chain: experiences from nanotoxicology. *Environ Sci Technol*. 2015;49(15):8932–47. <https://doi.org/10.1021/acs.est.5b01090>.
7. EFSA Panel on Food. Presence of microplastics and nanoplastics in food, with particular focus on seafood. *EFSA J*. 2016;14(6):e04501.
8. Toussaint B, Raffael B, Angers-Loustau A, Gilliland D, Kestens V, Petrillo M, et al. Review of micro- and nanoplastic contamination in the food chain. *Food Addit Contam Part A Chem Anal Control Expo Risk Assess*. 2019;36:639–73.
9. Ter Halle A, Jeanneau L, Martignac M, Jardé E, Pedrono B, Brach L, et al. Nanoplastic in the North Atlantic subtropical gyre. *Environ Sci Technol*. 2017;51(23):13689–97. <https://doi.org/10.1021/acs.est.7b03667>.
10. Hartmann NB, Hüffer T, Thompson RC, Hassellöv M, Verschoor A, Daugaard AE, et al. Are we speaking the same language? Recommendations for a definition and categorization framework for plastic debris. *Environ Sci Technol*. 2019;53(3):1039–47. Available from. <https://doi.org/10.1021/acs.est.8b05297>.
11. Venâncio C, Ferreira I, Martins MA, Soares AMVM, Lopes I, Oliveira M. The effects of nanoplastics on marine plankton: a case study with polymethylmethacrylate. *Ecotoxicol Environ Saf*. 2019;184:109632. <https://doi.org/10.1016/j.ecoenv.2019.109632>.
12. Gerdes Z, Hermann M, Ogonowski M, Gorokhova E. A novel method for assessing microplastic effect in suspension through mixing test and reference materials. *Sci Rep*. 2019;9(1):1–9.
13. Redondo-Hasselerharm PE, Falahudin D, Peeters ETHM, Koelmans AA. Microplastic effect thresholds for freshwater benthic macroinvertebrates. *Environ Sci Technol*. 2018;52(4):2278–86. <https://doi.org/10.1021/acs.est.7b05367>.
14. Nguyen B, Claveau-Mallet D, Hernandez LM, Xu EG, Farmer JM, Tufenkji N. Separation and analysis of microplastics and nanoplastics in complex environmental samples. *Acc Chem Res*. 2019;52(4):858–66. <https://doi.org/10.1021/acs.accounts.8b00602>.
15. Mintenig SM, Löder MGJ, Primpke S, Gerds G. Low numbers of microplastics detected in drinking water from ground water sources. *Sci Total Environ*. 2019;648:631–5. <https://doi.org/10.1016/j.scitotenv.2018.08.178>.
16. Schwaferts C, Niessner R, Elsner M, Ivleva NP. Methods for the analysis of submicrometer-and nanoplastic particles in the environment. *TrAC Trends Anal Chem*. 2019;112:52–65. <https://doi.org/10.1016/j.trac.2018.12.014>.
17. Gigault J, Ter Halle A, Baudrimont M, Pascal P-Y, Gauffre F, Phi T-L, et al. Current opinion: what is a nanoplastic? *Environ Pollut*. 2018;235:1030–4. <https://doi.org/10.1016/j.envpol.2018.01.024>.
18. Schwaferts C, Niessner R, Elsner M, Ivleva NP. Methods for the analysis of submicrometer- and nanoplastic particles in the environment. *Trends Anal Chem*. 2019;112:52–65. <https://doi.org/10.1016/j.trac.2018.12.014>.
19. Shim WJ, Hong SH, Eo SE. Identification methods in microplastic analysis: a review. *Anal Methods*. 2017;9(9):1384–91. <https://doi.org/10.1039/C6AY02558G>.
20. Materić D, Kasper-Giebl A, Kau D, Anten M, Greilinger M, Ludewig E, et al. Micro-and nanoplastics in alpine snow: a new method for chemical identification and (semi) quantification in the nanogram range. *Environ Sci Technol*. 2020;54(4):2353–9. <https://doi.org/10.1021/acs.est.9b07540>.
21. Enfrin M, Lee J, Gibert Y, Basheer F, Kong L, Dumée LF. Release of hazardous nanoplastic contaminants due to microplastics fragmentation under shear stress forces. *J Hazard Mater*. 2020;384:121393. <https://doi.org/10.1016/j.jhazmat.2019.121393>.
22. Sutherland KR, Madin LP, Stocker R. Filtration of submicrometer particles by pelagic tunicates. *Proc Natl Acad Sci*. 2010;107(34):15129–34. <https://doi.org/10.1073/pnas.1003599107>.
23. Randløv A, Riisgård H. Efficiency of particle retention and filtration rate in four species of ascidians. *Mar Ecol Prog Ser*. 1979;1:55–9. <https://doi.org/10.3354/meps001055>.
24. Jacobi Y, Yahel G, Shenkar N. Efficient filtration of micron and submicron particles by ascidians from oligotrophic waters. *Limnol Oceanogr*. 2018;63(S1):S267–79. <https://doi.org/10.1002/lno.10736>.
25. Hoshino Z, Tokioka T. An unusually robust Ciona from the northeastern coast of Honsyu Island, Japan; 1967.
26. Hurley RR, Lusher AL, Olsen M, Nizzetto L. Validation of a method for extracting microplastics from complex, organic-rich, environmental matrices. *Environ Sci Technol*. 2018;52(13):7409–17. <https://doi.org/10.1021/acs.est.8b01517>.
27. Courtene-Jones W, Quinn B, Murphy F, Gary SF, Narayanaswamy BE. Optimisation of enzymatic digestion and validation of specimen preservation methods for the analysis of ingested microplastics. *Anal Methods*. 2017;9(9):1437–45. <https://doi.org/10.1039/C6AY02343F>.
28. Mintenig SM, Bäuerlein PS, Koelmans AA, Dekker SC, Van Wezel AP. Closing the gap between small and smaller: towards a framework to analyse nano- and microplastics in aqueous environmental samples. *Environ Sci Nano*. 2018;5(7):1640–9. <https://doi.org/10.1039/C8EN00186C>.
29. Correia M, Loeschner K. Detection of nanoplastics in food by asymmetric flow field-flow fractionation coupled to multi-angle light scattering: possibilities, challenges and analytical limitations. *Anal Bioanal Chem*. 2018;410(22):5603–15. <https://doi.org/10.1007/s00216-018-0919-8>.
30. Gigault J, El Hadri H, Reynaud S, Deniau E, Grassl B. Asymmetrical flow field flow fractionation methods to characterize submicron particles: application to carbon-based aggregates and nanoplastics. *Anal Bioanal Chem*. 2017;409(29):6761–9. <https://doi.org/10.1007/s00216-017-0629-7>.
31. Gigault J, Hackley VA. Differentiation and characterization of isotopically modified silver nanoparticles in aqueous media using asymmetric-flow field flow fractionation coupled to optical detection and mass spectrometry. *Anal Chim Acta*. 2013;763:57–66. <https://doi.org/10.1016/j.aca.2012.11.060>.
32. El Hadri H, Louie SM, Hackley VA. Assessing the interactions of metal nanoparticles in soil and sediment matrices—a quantitative analytical multi-technique approach. *Environ Sci Nano*. 2018;5(1):203–14. <https://doi.org/10.1039/C7EN00868F>.
33. Facchetti SV, La Spina R, Fumagalli F, Riccardi N, Gilliland D, Ponti J. Detection of metal-doped fluorescent PVC microplastics in freshwater mussels. *Nanomaterials*. 2020;10(12):2363. <https://doi.org/10.3390/nano10122363>.
34. Andersson M, Wittgren B, Wahlund K-G. Accuracy in multiangle light scattering measurements for molar mass and radius estimations. Model calculations and experiments. *Anal Chem*. 2003;75(16):4279–91. <https://doi.org/10.1021/ac030128+>.
35. Verkouteren RM, Verkouteren JR. Inkjet metrology II: resolved effects of ejection frequency, fluidic pressure, and droplet number on reproducible drop-on-demand dispensing. *Langmuir*. 2011;27(15):9644–53. <https://doi.org/10.1021/la201728f>.
36. Gigault J, Pettibone JM, Schmitt C, Hackley VA. Rational strategy for characterization of nanoscale particles by asymmetric-flow field flow fractionation: a tutorial. *Anal Chim Acta*. 2013;809:9–24.
37. Gigault J, Pettibone JM, Schmitt C, Hackley VA. Rational strategy for characterization of nanoscale particles by asymmetric-flow field flow fractionation: a tutorial. *Anal Chim Acta*. 2014;809:9–24. <https://doi.org/10.1016/j.aca.2013.11.021>.
38. Clogston JD, Hackley VA, Prina-Mello A, Puri S, Sonzini S, Soo PL. Sizing up the next generation of nanomedicines. *Pharm Res*. 2020;37(1):1–10.
39. Donaldson SH Jr, Røyne A, Kristiansen K, Rapp MV, Das S, Gebbie MA, et al. Developing a general interaction potential for hydrophobic and hydrophilic interactions. *Langmuir*. 2015;31(7):2051–64. <https://doi.org/10.1021/la502115g>.
40. Eklöf J, Gschneidner T, Lara-Avila S, Nygård K, Moth-Poulsen K. Controlling deposition of nanoparticles by tuning surface charge of SiO₂ by surface modifications. *RSC Adv*. 2016;6(106):104246–53. <https://doi.org/10.1039/C6RA22412A>.
41. Herdman WA. L.M.B.C. memoirs on typical British marine plants and animals. Vol. 1. Ascidia. Liverpool: Liverpool University Press; 1899. 78 p.
42. Shrestha S, Wang B, Dutta P. Nanoparticle processing: understanding and controlling aggregation. *Adv Colloid Interf Sci*. 2020;279:102162. <https://doi.org/10.1016/j.cis.2020.102162>.

Publisher's Note

Springer Nature remains neutral with regard to jurisdictional claims in published maps and institutional affiliations.